

Article

Effects of FSW Tool Plunge Depth on Properties of an Al-Mg-Si Alloy T-Joint: Thermomechanical Modeling and Experimental Evaluation

Shabbir Memon ¹, Dariusz Fydrych ², Aintzane Conde Fernandez ³, Hamed Aghajani Derazkola ³
and Hesamoddin Aghajani Derazkola ^{4,*}

¹ Department of Mechanical Engineering, Wichita State University, Wichita, KS 67260-133, USA; sxmemon@shockers.wichita.edu

² Institute of Machines and Materials Technology, Faculty of Mechanical Engineering and Ship Technology, Gdańsk University of Technology, Gabriela Narutowicza Street 11/12, 80-233 Gdańsk, Poland; dariusz.fydrych@pg.edu.pl

³ Department of Mechanics, Design and Industrial Management, University of Deusto, Avda Universidades 24, 48007 Bilbao, Spain; aintzane.conde@deusto.es (A.C.F.); h.aghajani@deusto.es (H.A.D.)

⁴ Department of Mechanical Engineering, University of Mazandaran, Babolsar 47415, Iran

* Correspondence: h.aghajani@live.com



Citation: Memon, S.; Fydrych, D.; Fernandez, A.C.; Derazkola, H.A.; Derazkola, H.A. Effects of FSW Tool Plunge Depth on Properties of an Al-Mg-Si Alloy T-Joint: Thermomechanical Modeling and Experimental Evaluation. *Materials* **2021**, *14*, 4754. <https://doi.org/10.3390/ma14164754>

Academic Editor: Jan Haubrich

Received: 3 August 2021

Accepted: 20 August 2021

Published: 23 August 2021

Publisher's Note: MDPI stays neutral with regard to jurisdictional claims in published maps and institutional affiliations.



Copyright: © 2021 by the authors. Licensee MDPI, Basel, Switzerland. This article is an open access article distributed under the terms and conditions of the Creative Commons Attribution (CC BY) license (<https://creativecommons.org/licenses/by/4.0/>).

Abstract: One of the main challenging issues in friction stir welding (FSW) of stiffened structures is maximizing skin and flange mixing. Among the various parameters in FSW that can affect the quality of mixing between skin and flange is tool plunge depth (TPD). In this research, the effects of TPD during FSW of an Al-Mg-Si alloy T-joint are investigated. The computational fluid dynamics (CFD) method can help understand TPD effects on FSW of the T-joint structure. For this reason, the CFD method is employed in the simulation of heat generation, heat distribution, material flow, and defect formation during welding processes at various TPD. CFD is a powerful method that can simulate phenomena during the mixing of flange and skin that are hard to assess experimentally. For the evaluation of FSW joints, macrostructure visualization is carried out. Simulation results showed that at higher TPD, more frictional heat is generated and causes the formation of a bigger stir zone. The temperature distribution is antisymmetric to the welding line, and the concentration of heat on the advancing side (AS) is more than the retreating side (RS). Simulation results from viscosity changes and material velocity study on the stir zone indicated that the possibility of the formation of a tunnel defect on the skin–flange interface at the RS is very high. Material flow and defect formation are very sensitive to TPD. Low TPD creates internal defects with incomplete mixing of skin and flange, and high TPD forms surface flash. Higher TPD increases frictional heat and axial force that diminish the mixing of skin and flange in this joint. The optimum TPD was selected due to the best materials flow and final mechanical properties of joints.

Keywords: friction stir welding; Al-Mg-Si alloy; T-joint configuration; tool plunge depth; thermomechanical simulation

1. Introduction

Stiffness structures such as T-joints are an exciting topic for automobile and aerospace manufacturers [1–3]. Between metallic alloys, Al-Mg-Si significantly decreases engineering weight and improves the strength of structures [4]. Due to the benefits of Al-Mg-Si such as good tensile strength, good corrosion properties, and weldability, these alloys are considered for use in lightweight automobile structures to diminish fuel usage [5]. In the past, many researchers considered the production of T-joints with the various conventional welding processes. These joints had many defects during traditional welding processes [6–10].

With the benefits of the new emerging solid-state joining process, the number of defects is decreased, and joint size is decreased [11]. The formation of smaller joint sizes causes lower metallurgical and chemical changes in base materials, leading to stronger joints [12]. T-shape joints consist of two structural parts called skin and stringer (flange). The skin is placed horizontally, and the flange is added vertically to the skin [13]. One of the most effective solid-state joining technologies is friction stir welding (FSW), which can improve the final properties of the welded joint compared to traditional joining techniques [14]. The FSW process is capable of welding various materials and geometries. With the FSW process, the final welding properties can retain up to 90% of base material features such as aluminum alloys [15]. During the joining process of T-configuration structures, the most critical factor is the optimal mixing of the skin and flange without defects [16]. Internal voids and material explosions are common defects that directly affect the strength of FSW T-joints [13]. In comparison with other configuration joints, it was found that the final properties of T-configuration joints have a higher sensitivity to FSW parameters. Among the various technical process parameters in the FSW process, tool plunge depth (TPD) has a significant effect on internal material flow and defect formation [17,18]. It is worth mentioning that previous studies mainly considered aspects related to heat input optimization and ignored the importance of TPD effects during T-joint structure production [19,20]. Low TPD decreases friction contact between the tool and the workpiece, and high TPD decreases SZ size due to the formation of high surface flash around the joint line. Thus, optimization of TPD to analyze material flow and avoid void formation is critical [7,21,22].

Simulations were carried out to understand frictional heat generation, strain rate, and the prediction of defect formation during friction stir welding of a T-joint. Simulation of the FSW process with the computational fluid dynamics (CFD) technique provides reliable and comprehensive details for the analysis of frictional heat generation, temperature distribution, and the flow of stirred materials during and after the FSW process. To date, published literature on FSW of a T-joint has focused on optimizing FSW tool rotational and traveling speeds [23–25]. On the other hand, there are limited studies that simulated FSW of a T-joint. This research aims to study TPD effects on the temperature, strain rate, and material behavior of an Al-Mg-Si lap T-joint configuration by 3D simulation and experimental investigation.

2. Materials and Methods

The welding procedure was performed with a friction stir welding modified milling machine (Tabriz TZ14/5). The raw materials were cut from an AA6068 aluminum alloy (Aform, Arak, Iran) sheet. The specimens were prepared with dimensions of 100 mm × 200 mm × 4 mm for the skin and 100 mm × 50 mm × 4 mm for the flange. The chemical composition and mechanical properties of AA6068 aluminum alloy used in this study are presented in Tables 1 and 2. Determination of the chemical composition was performed by emission spectroscopy (Hitachi, Japan) according to the ASTM E415 [13]. For the micrographic analysis of joint surface flow, an optical camera (Canon, Huntington, NY, USA) was used.

Table 1. AA6082 aluminum alloy mechanical properties.

Parameter	Density	Melting Point	Thermal Conductivity	Ultimate Tensile Strength	Shear Stress	Elongation	Vickers Hardness
Unit	kg/m ³	°C	W/m.K	MPa	MPa	%	HB
Value	2700	555	180	300	460	10	91

Table 2. AA6068 aluminum alloy chemical composition.

Element	Cu	Mg	Mn	Si	Fe	Cr	Zn	Al
Wt.%	0.1	1.2	1	1.3	0.5	0.25	0.2	balance



In the experimental process design, the flange was located in the center of the skin in the fixture. Steel was made using fixtures for locating base metals during the joining process. During the welding process, TPD was selected as a variable, and other factors remained constant to find the effect of a given parameter. With a trial-and-error testing plan, optimum values of FSW tool parameters such as velocity, offset, and tilt angle were selected. During the experimental procedure, all parameters were kept constant in order to find the effects of TPD on the properties of the final joint. The plan of process parameters in this study is presented in Table 3. The minimum and maximum TPDs were selected according to the geometrical limitation. The initial TPDs selected were 0 mm when the tool shoulder was in contact with the skin’s surface, and it was not possible for the maximum value to be more than 0.5 mm because the pin was broken during forward movement of the tool. A tungsten-carbide tool (Zigong Xingyu Technicarbide, Zigong, China) with a conical frustum pin was used for welding. FSW tool geometry and dimensions are presented in Figure 1a. The size of the tool was selected according to the geometrical limitations of aluminum alloy sheets. Two K-type thermocouples (TC1 and TC2) were positioned in the FSW tool to record thermal changes in the joint line. Thermocouple positions in the FSW tool are depicted in Figure 1a. To monitor heat distribution during the FSW process, three K-type thermocouples (Omega Engineering, Norwalk, CT, USA) were positioned on the AS and RS on the skin, and two thermocouples were used on the flange. A schematic cross-sectional view of thermocouple positions is depicted in Figure 1b.

Table 3. Welding process parameters.

Parameter	Tool Rotation Speed	Welding Speed	Tool Tilt Angle	Tool Plunge Depth	Tool Offset
Sample Number	rpm	mm/min	degree	mm	mm
1	1400	40	2	0	+0.2
2	1400	40	2	0.1	+0.2
3	1400	40	2	0.2	+0.2
4	1400	40	2	0.3	+0.2
5	1400	40	2	0.4	+0.2
6	1400	40	2	0.5	+0.2

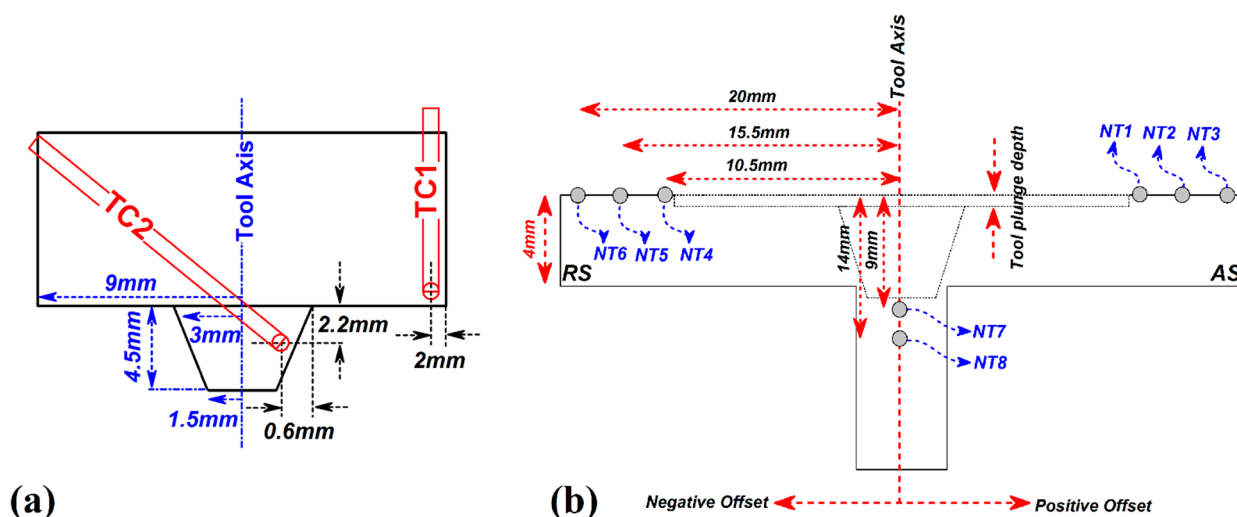


Figure 1. Schematic view of thermocouple position on (a) FSW tool and (b) skin and flange side.

During monitoring of thermal history, data from the thermocouples were transferred to an ADAM-4018+ module (Advantech, Irvine, CA, USA). After that, thermocouple data were monitored by LabView software on a computer. In this study, Z- and X-forces of the FSW tool were measured with a strain-gauge-based load cell (Mavin, Xiamen, China) to

better analyze the effects of TPD on material flow. A programmable logic controller (PLC) system (MZ3P, Shenzhen Coolmay Technology, China) controlled the forces, and the system was integrated with a personal desktop computer and LabView software for data acquisition. Metallographic investigation was performed by the optical microscopic (OM) model CX43 (Olympus, Okaya, Japan) equipped with image analysis software (ImageJ, USA) to measure the microstructure size. A small sample was cut from the middle of the welded samples, and after refining by sandpaper number 100 (Trading Company, Yichang, China) until 2000 (Trading Company, Yichang, China), the prepared samples were polished by diamond paste (Liqui Moly, Ulm, Germany). In the last step, the microstructure samples were chemically etched by 2% HF, 2% HBF₄, 48% ethanol, and 48% H₂O solution. The test was repeated three times for each welding condition, and their average values were reported. For the use of flow stress of the base metal at different temperatures in the simulation procedure, uniaxial tension tests were performed on AA6068 aluminum alloy from 25 °C up to 500 °C according to ASTM E21 [13]. Thermal conductivity and specific heat of AA6068 aluminum alloy were measured according to ASTM E1461 and the results used in the simulation procedure [13].

3. Process Modeling

The simulation domain in this study was determined according to the actual situation in the experimental procedure. A 3D, steady-state, single-phase-flow CFD model was established. A moving reference method was employed to investigate the thermomechanical features around the welding tool. The origin of rotation (model reference) was on the FSW tool axis. Mass, momentum, and energy conservation equations used in this simulation are presented as [25]:

Mass conservation:

$$s_{i,i} = 0 \quad (1)$$

The momentum conservation equation is presented as [26]:

$$\rho(s_i s_j)_{,i} = -F_j + \mu(s_{i,ij} + s_{j,ii}) - \rho S_1 s_{j,1} \quad (2)$$

In Equation (2), μ is non-Newtonian viscosity. μ can be determined from Al-Mg-Si alloy flow stress (σ_e) divided by the effective strain rate, which can be presented as [11]:

$$\mu = \frac{\sigma_e}{3\dot{\epsilon}} \quad (3)$$

The flow stress in Equation (3) is defined as [27]:

$$\sigma_e = \frac{1}{\alpha} \operatorname{arcsinh} \left(\frac{Z}{A} \right)^{\frac{1}{n}} \quad (4)$$

A , α , and n are material constants that can be obtained from the stress–strain of aluminum alloy at different temperatures (Figure 2a), and Z is the Zener–Hollomon parameter. The Zener–Hollomon parameter represents the temperature-compensated effective strain rate [28]:

$$Z = \dot{\epsilon} \exp \left(\frac{Q}{RT} \right) \quad (5)$$



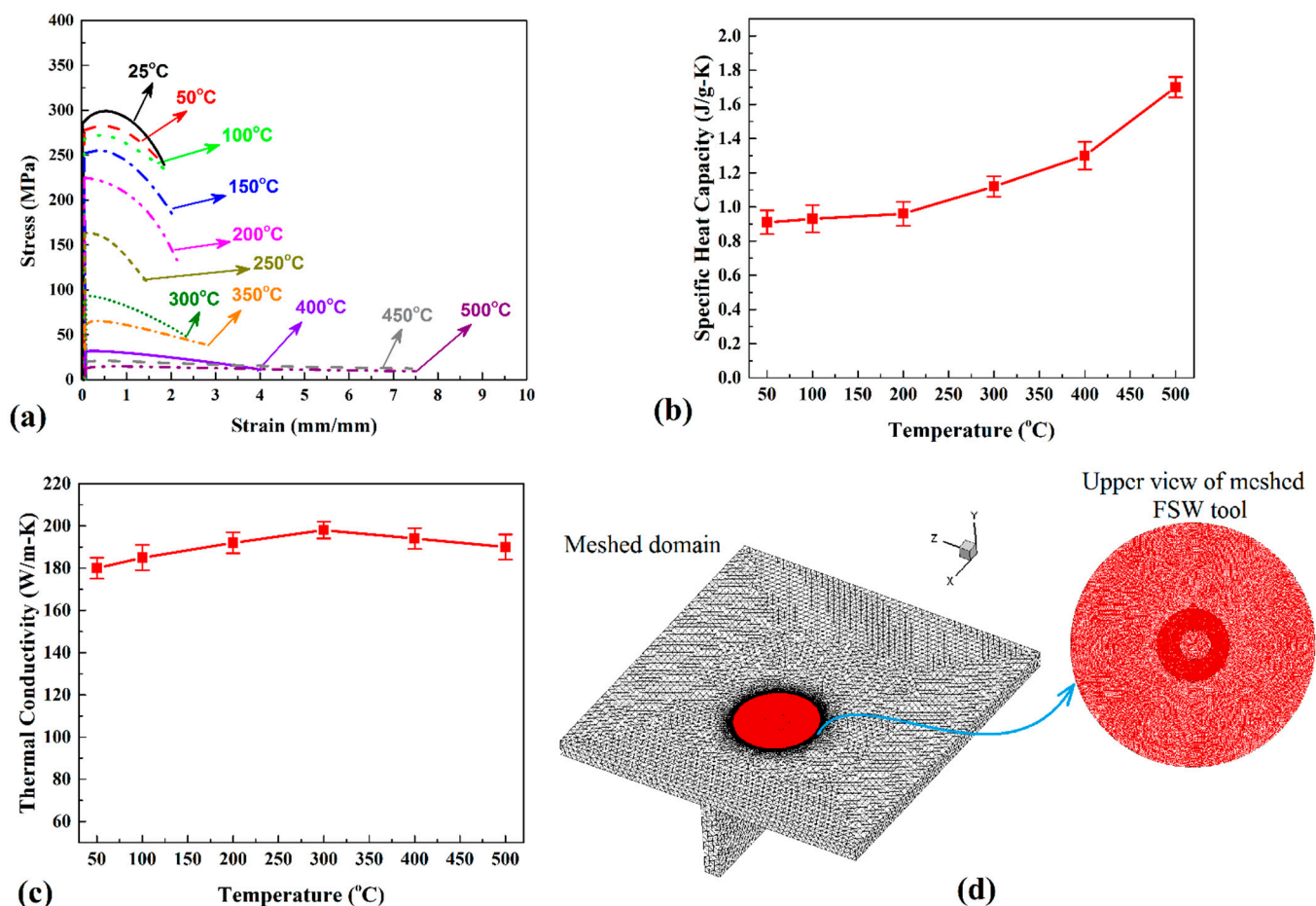


Figure 2. (a) Stress–strain graph of AA6068 aluminum alloy at various temperatures. (b) Specific heat and (c) thermal conductivity of AA6068 aluminum alloy at various temperatures. (d) Meshed domain.

$Q = 158.3$ kJ/mol is the activation energy [29], R is the universal gas constant, and $\dot{\epsilon}$ is the effective strain rate, which is defined as [30]:

$$\dot{\epsilon} = \sqrt{\frac{2}{3} \epsilon_{ij} \epsilon_{ij}} \quad (6)$$

ϵ_{ij} is the strain rate tensor, defined as [31]:

$$\epsilon_{ij} = \frac{1}{2} \left(\frac{\partial s_i}{\partial x_j} + \frac{\partial s_j}{\partial x_i} \right) \quad (7)$$

The energy conservation equations attached to them could be defined as [32]:

$$\rho C_p \frac{\partial (s_i T)}{\partial x_i} = -\rho C_p S_1 \frac{\partial T}{\partial x_1} + \frac{\partial}{\partial x_i} \left(k \frac{\partial T}{\partial x_i} \right) + G_i + G_b \quad (8)$$

G_i and G_b are the total generated heat by friction and plastic deformation, respectively, at the interface of the tool and workpiece.

The generated heat by friction (G_i) at the tool–workpiece interface is presented as [33]:

$$G_i = \left[(1 - \gamma) \kappa \tau + \gamma \mu_f P_N \right] (\omega r - S_1 \sin \theta) \quad (9)$$

where θ is the angle of tool surfaces with the x -axis, κ is the mechanical efficiency factor, and γ is the fractional slip factor at the interfaces. G_b , in Equation (8), is presented as [34]:

$$G_b = \frac{d\dot{\epsilon}_p}{dV} = \beta\mu\chi \quad (10)$$

χ is defined by [15]:

$$\chi = 2 \sum_{i=1}^3 \left(\frac{\partial s_i}{\partial x_i} \right)^2 + \left(\frac{\partial s_1}{\partial x_2} + \frac{\partial s_2}{\partial x_1} \right)^2 + \left(\frac{\partial s_1}{\partial x_3} + \frac{\partial s_3}{\partial x_1} \right)^2 + \left(\frac{\partial s_3}{\partial x_2} + \frac{\partial s_2}{\partial x_3} \right)^2 \quad (11)$$

In Equation (10), β is a factor that indicates the extent of mixing on the atomic scale. The value of β is defined between 0 and 1, where 0 is used for a nonmixing situation, and 1 is used for a well-mixed situation. The percentage of heat transferred into the workpiece is related to the thermal conductivity, density, and heat capacity of both the tool and workpiece material and is calculated by [35]:

$$\gamma = \frac{(\sqrt{k\rho C_p})_{workpiece}}{(\sqrt{k\rho C_p})_{tool} + (\sqrt{k\rho C_p})_{workpiece}} \quad (12)$$

The heat flux continuity of the shoulder–workpiece interface is presented as [36]:

$$k \frac{\partial T}{\partial Z} \Big|_{Top} = \varphi q \quad (13)$$

q is the heat generation rate of the shoulder–workpiece interface. The value of heat transfer at the bottom of the workpiece can be defined by [37]:

$$k \frac{\partial T}{\partial Z} \Big|_{Bottom} = h_b(T - T_a) \quad (14)$$

In Equation (14), h_b is the bottom heat transfer coefficient, and T_a is the ambient temperature (298 K). The heat transfer coefficient at the bottom face depends on the local temperature and is given by the following relation [38]:

$$h_b = h_{b0}(T - T_a)^{0.25} \quad (15)$$

In Equation (15), h_{b0} is the heat transfer parameter for the bottom surface of the workpiece. Heat transfer at the top surface of the workpiece consists of both convection and radiation given by [39]:

$$-k \frac{\partial T}{\partial Z} \Big|_{Top} = B\epsilon(T^4 - T_a^4) + h_t(T - T_a) \quad (16)$$

During this simulation, the mechanical properties of the workpiece are defined concerning temperature. To increase the accuracy of the simulation, specific heat (C_p) and thermal conductivity (K) of AA6068 aluminum alloy at different temperatures were used according to the results of the experimental tests (Figure 2b,c) and, similarly, for the tungsten-made FSW tool [40–43]:

$$C_p = 468.3 - 8.5T + 3.0 \times 10^{-4}T^2 + 1.8 \times 10^{-7}T^3 \quad (17)$$

$$K = 3.8 + 0.092T - 1.8 \times 10^{-4}T^2 + 7.8 \times 10^{-8}T^3 \quad (18)$$

In this simulation, the CFD package of commercial Ansys Workbench software (ANSYS, Inc., Canonsburg, PA, USA) was implemented. Thermomechanical properties of aluminum alloy were imported to the software by subroutine codes. Al-Mg-Si alloy was considered as a non-Newtonian fluid with viscoelastic behavior. A 3D view of the meshed domain and the stir zone is depicted in Figure 2d. The simulation results are compared with the recorded thermal results. In all results, the maximum error of simulation results and experimental results is lower than 3%.

4. Results and Discussions

4.1. Thermal Study

In the FSW process, the produced frictional heat directly affects the properties and working life of the final joints [44]. The temperature distribution and generated heat determine the material flow during forward movement of the FSW tool, defect mechanism, microstructural changes, and mechanical properties of the joint. Optimal frictional heat generation is required to obtain good material flow.

Generally, the total heat in FSW is due to the generation of friction at the tool-workpiece interface, which deforms the plasticity of the raw metal [45]. The heat generated by plastic deformation is related to the material's resistance against deformation, creating internal frictional forces [46]. To better understand the relationship between TPD and total heat generation, as an example, the temperatures recorded by TC1 and TC2 (inside the tool) and the NT1-NT8 of the welded joint at 0.2 mm TPD are presented in Figure 3a,b, respectively. The results show that heat produced on the shoulder side is more than on the pin side.

This behavior is recorded for all samples. The recorded temperature of the shoulder (~498 °C) is more than 150 °C on the pin side (~368 °C). The recorded heat in TC2 is a combination of produced heat in the skin and flange by the pin. The recorded temperature on the surface of base metals at the skin and flange is shown in Figure 3c. The recorded temperature by thermocouples on the skin (NT1-NT5) is less than TC1-TC2. It seems the difference is due to the thermal conductivity of eth SZ with the tool body and backing plate. Recorded temperatures at 0, 0.1, 0.2, 0.3, 0.4, and 0.5 mm TPDs are 468 °C, 479 °C, 498 °C, 512 °C, 520 °C, and 541 °C, respectively. It seems with increasing TPD, frictional heat growth is due to higher axial force on the SZ [18]. A cross-sectional view of the simulation results of heat distribution at various TPDs is depicted in Figure 3d. As can be seen, with increasing TPD, the generated heat increases, and more heat is diffused into the flange. The distribution of heat in the joint's longitudinal section revealed heat flux in the skin and flange was nonhomogenous. Due to the tool's rotational direction, the heat distribution on the AS is more than the RS in all cases. The distribution of heat is predicted comprehensively on the flange side. The simulation results show that the generated temperatures at 0, 0.1, 0.2, 0.3, 0.4, and 0.5 mm TPD are 462 °C, 473 °C, 492 °C, 506 °C, 512 °C, and 535 °C, respectively. On closer inspection, the percentage of generated heat on the flange side is near 23% at 0 mm TPD (minimum) to 27% at 0.5 mm TPD (maximum) compared to the total generated heat. With increasing TPD, the contact area between the flange and pin increases and, consequently, generates heat with the flange. The statically results predicted that the FSW tool's total heat increased at higher TPD, and the percentage of generated heat in the flange increased at higher TPD. This phenomenon is related to the contact area between the tool pins, with the flange at higher TPD (Figure 3e). From a geometrical perspective, the contact area between the FSW pin and flange increases at higher TPD. On the shoulder side, with increasing TPD, the axial force increases the contact pressure on the contact area between the shoulder and workpiece in the skin.

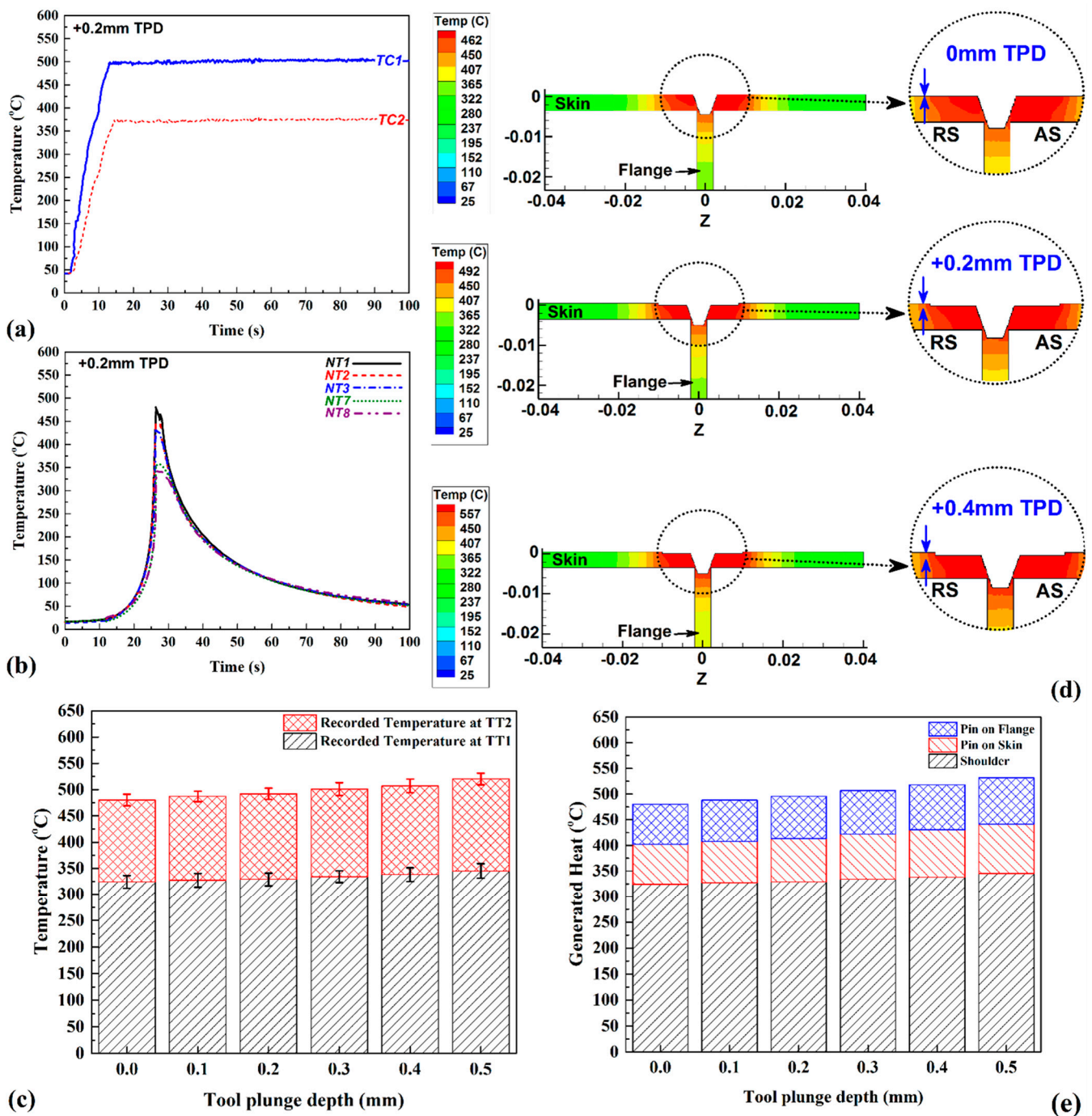


Figure 3. (a) Recorded temperature inside the FSW tool. (b) Recorded surface temperature of the joint. (c) Recorded temperature inside the FSW tool at various TPDs. (d) Cross-sectional view of the simulation results of internal heat flow. (e) Simulation results of generated heat at various TPDs.

The simulation results of heat distribution on the longitudinal section and top surface of a 0.2 mm TPD joint are depicted in Figure 4a,b, respectively. The points selected to record temperature from the simulation results are located at the same position as the thermocouples in the workpieces. The recorded temperature from the thermocouples around the joint line at the skin and simulation results are presented in Figure 4c,d. The maximum heat was recorded at 0.5 mm TPD and the minimum at 0 mm TPD. The simulation results were in good agreement with the recorded data. The recorded temperature on the flange side (Figure 4e) reveals that the generated heat in the lower areas of SZ is much lower than in the upper area. Due to the direct contact of the shoulder with the skin (which leads

to more contact area compared to the pin), heat generated in the upper area is increased. The NT1 at the AS of the skin, NT4 at the RS of the skin, and NT5 at the flange side were recorded at a maximum temperature around the SZ [47]. The other data recorded in the thermocouples can be used to monitor heat diffusion inside the aluminum alloy. The obtained results reveal that the heat flow gradient on the flange side is more than the skin. This phenomenon means the heat flow in the flange is faster than in the skin. However, the materials used are the same. The geometry of the flange being narrower and thinner than in the skin means that the heat flux in the flange is faster than in the skin.

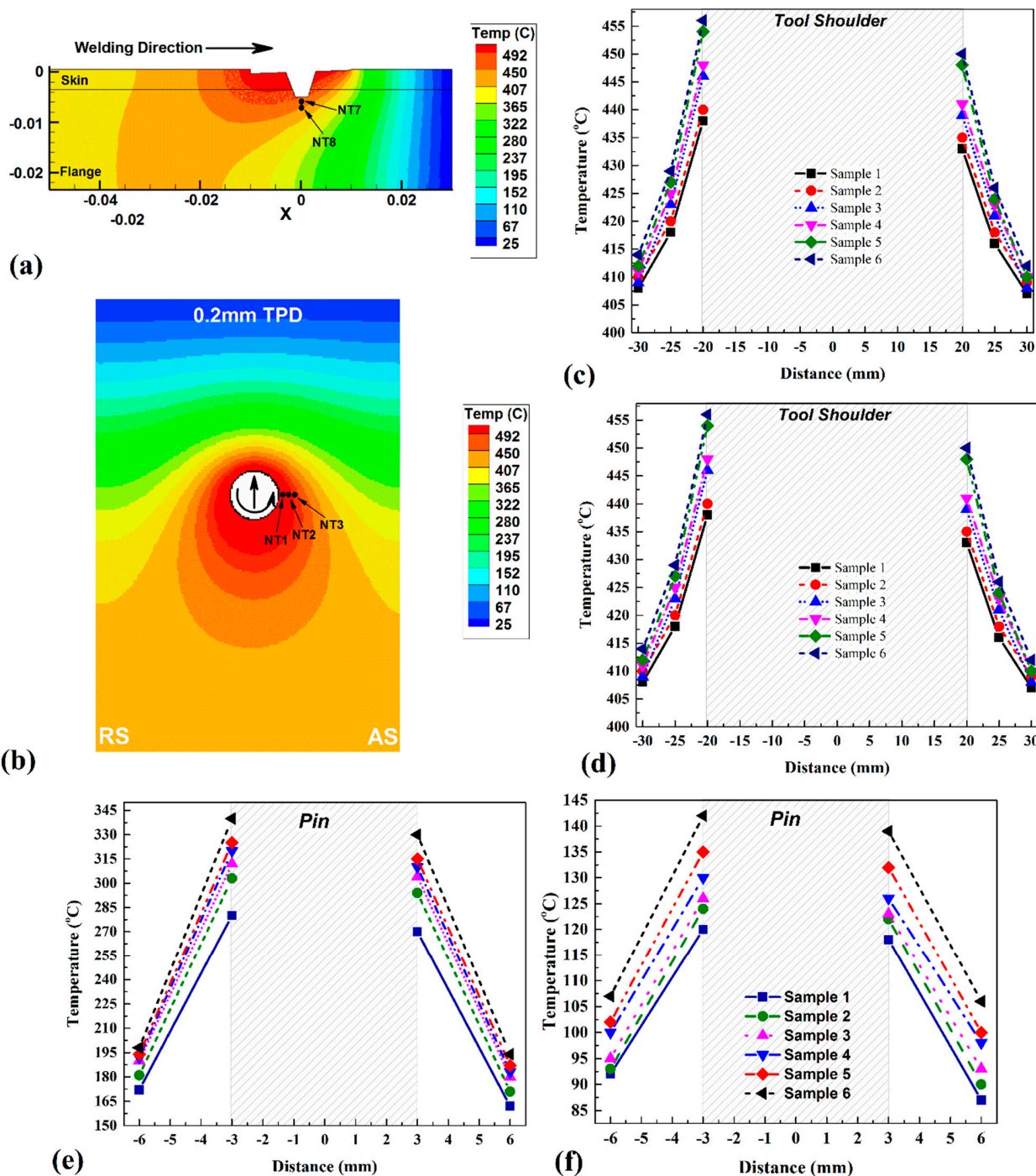


Figure 4. (a) Simulation results of internal heat flow at 0.2 mm TPD. (b) Simulation results of internal heat flow at 0.2 mm TPD. (c) Experimental and (d) maximum simulated temperature and heat diffusion on skin. (e) Recorded and (f) simulated results of maximum temperature and heat diffusion on flange.

4.2. Viscosity and Force Analysis

During the simulation, the plasticized metal with low shear strength is referred to as metal viscosity [48]. According to experimental tests and simulations in the literature, material overflow occurs when the base metal viscosity is very low. It has been proven that the viscosity of the base metal during the FSW process should decrease until the workpiece is converted to a plasticized form. At this point, the FSW tool would be able to plastic stirring flow and mix raw materials. Material viscosity is a robust local strain rate and temperature during thermomechanical simulation of the FSW process. Figure 5a shows a longitudinal section view of the simulation results of the viscosity changes of Al-Mg-Si alloy around the SZ. With increasing TPD and heat input growth in the SZ, aluminum's shear strength decreases, and the stirring action of Al-Mg-Si increases [49].

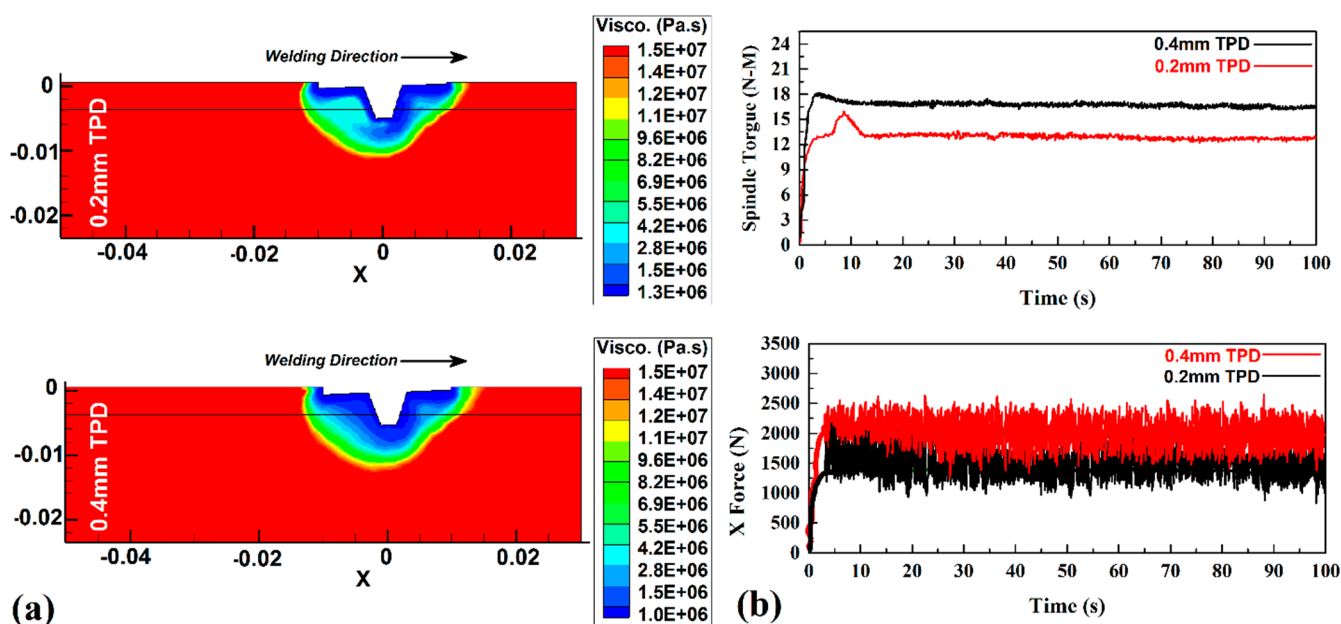


Figure 5. (a) Simulation results of internal viscosity changes at 0.2 mm and 0.4 mm TPD. (b) Force analysis of the FSW tool at 0.2 mm and 0.4 mm.

For this reason, material viscosity (shear strength) decreased at high TPD. The high viscosity of base metals at lower TPD prevents the formation of appropriate stirring action. On the other hand, enough frictional heat can completely plasticize the base metal and create a good mixture. The simulation result shows that the viscosity at the interface of the skin and flange is low at low TPD. Thus, a tunnel defect formed at the flange–skin interface at low TPD.

Figure 5b represents variations in the axial force (Z-force) and applied force on the tool (X-force) during the FSW process. The recorded results indicated that both X-force and Z-force increased with increasing TPD. The results revealed that a smooth spindle torque and vertical force distribution occur during FSW at lower TPD. This result indicates more material flow may have been achieved after a particular threshold value of TPD as X and Z-force [50–53]. On the other hand, higher Z-force at high TPD increased over material flow during the welding procedure. The greater contact area between the FSW tool shoulder and Al-Mg-Si alloy leads to material explosion from the joint line and forms a surface flash [22].

4.3. Velocity of Materials

The frictional heat decreases the viscosity of raw materials, and with the rotating FSW tool, the plasticized workpiece starts to rotate with the tool's rotational direction [18]. The material's velocity indicates how the surface or internal flow forms. The material velocity in the joint line results from radial stresses that are applied by the tool. Material velocity is the result of Al-Mg-Si plasticization, which allows the raw material to rotate inside the SZ by tool rotation movement. By increasing frictional heat, the shear strength (viscosity) of Al-Mg-Si decreases, and the SZ material's speed increases. Radiographic tests revealed that missing materials occurred at high TPD on the crown of the joint line. This phenomenon is caused by the tool's high plunging, which prevents material movement from the RS into the AS during the tool's forward movement [54]. This prevention can be caused by surface flash at the vicinity of the joint line [55]. Figure 6a shows the surface flow at 0.2 mm TPD and 0.4 mm TPD. As can be seen, the big surface flash formed around the joint line.

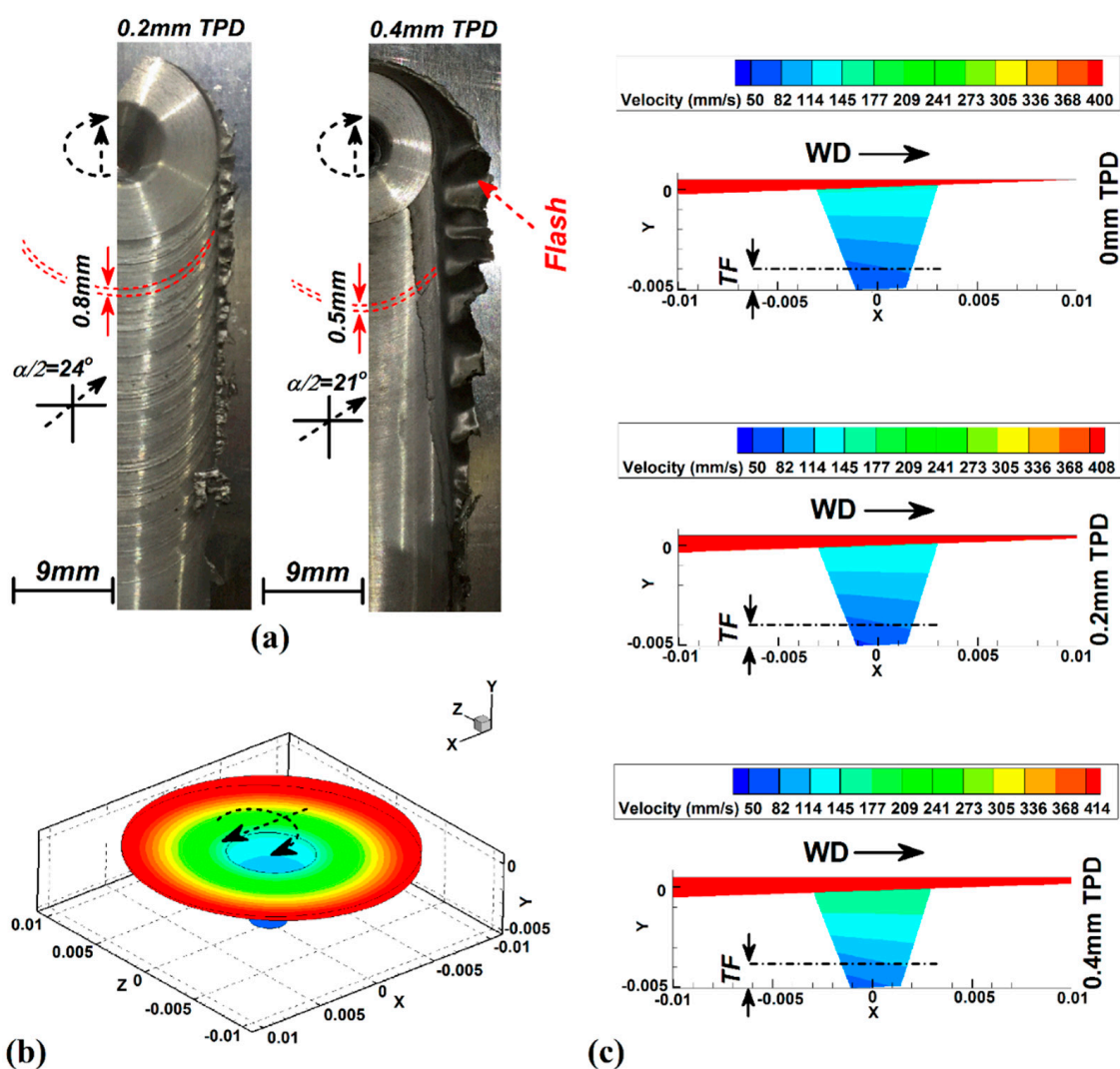


Figure 6. (a) Surface materials flow at 0.2 mm and 0.4 mm TPD. (b) Three-dimensional (3D) view of material velocity from simulation result. (c) Side view from velocity simulation result of various TPD.

The material's velocity magnitude in the SZ is not the same as the rotational velocity of the FSW tool. Material velocity in the SZ is a mixing action caused by the FSW tool (Figure 6b). This phenomenon, known as stirring action, provides valuable information about the internal defect formation [56–58]. The controlling stirring action during FSW of the T-configuration is essential to produce a sound joint [3,19,36,59]. The material velocity can change the share of the flange in the welding area. The contribution of the skin and flange in the formation of the SZ can affect the mechanical properties of the joint [19]. Hence, the geometrical valuation showed that, with increasing TPD, the contact surface between the FSW tool pin and flange (TF) is increased. The thermal study discovered that with increasing TPD, frictional heat is produced by the pin growth. With decreasing TPD, frictional heat and material velocity decrease. At lower TPD, the FSW tool cannot diminish the shear strength of Al-Mg-Si alloy, and mixing between the skin and flange is incomplete.

Figure 6c presents the simulation results of material velocity at 0.2 mm TPD and a side view of material velocity at different TPDs. As discussed earlier, with increasing TPD, the velocity of materials in SZ increases.

4.4. Strain Rate and Microstructure

The longitudinal section view of the strain rate simulation results is shown in Figure 7a. Due to obtained results, with increasing TPD (heat input in SZ), the strain rate increased [60]. With increasing contact area between the FSW tool's pin and flange at higher TPD, the flange side has a higher strain rate [61–63]. With increasing TPD, the more softening phenomena that occur. The strain rate changes affected the stirring materials in the SZ and shifted the thermomechanical-affected zone (TMAZ) and heat-affected zone (HAZ) areas on the flange side [64]. Higher heat concentration (as a result of higher heat generation) increases plasticization of the metal at high TPD and leads to a higher strain rate in the SZ. The microstructure of samples welded at 0.2 mm and 0.4 mm TPD is depicted in Figure 7b. Because the joint line was not formed at 0.4 mm TPD, a specific area in the RS was selected, indicating microstructural changes. Static analysis of the joint size of all samples is depicted in Figure 7c. The results show that with increasing TPD, the size of the SZ increases to 0.2 mm TPD. With increasing TPD more than 0.2 mm and the formation of internal defects, the size of the SZ decreases. This trend is observed in TMAZ size as well. Because defects were not formed in the HAZ area, the average size of the HAZ in the skin and flange has a growing trend with increasing TPD [65].

The geometry of the final joint directly relates to the morphology of the SZ and TMAZ [10,23,66,67]. Due to the obtained results, the SZ and TMAZ are small in the joints that were not formed completely. The biggest SZ and TMAZ are formed in 0.2 mm TPD with 33 mm² and 9 mm² areas, respectively. The HAZ area does not relate to the geometry of the joint area. As seen with increasing heat input, the size of the HAZ increased gradually. The results revealed that finer grain sizes form in the SZ of joints than FSW at higher TPD. The simulation results indicated that a higher strain rate in the SZ decreased the microstructure size (Figure 7d). According to the results, the immense grain size is formed in the SZ at 0 mm TPD (~15 µm), and the smallest grain size is formed in the SZ at 0.4 mm TPD (~10 µm). The final size of the microstructure is determined by the average heat input, material velocity, and strain rate.



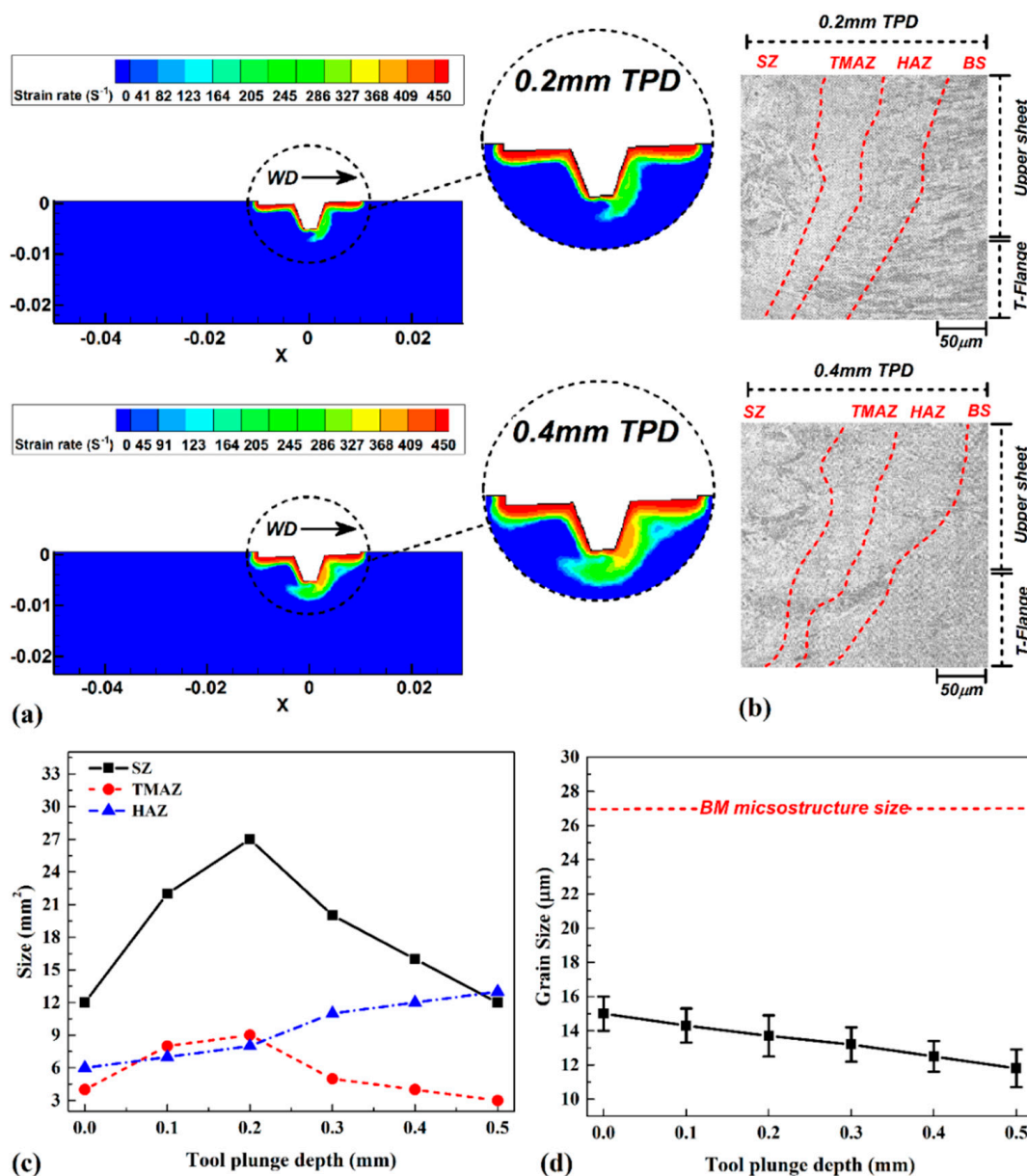


Figure 7. (a) Simulation results of strain rate in 0.2 mm and 0.4 mm TPD joints. (b) Microstructure of SZ in 0.2 mm and 0.4 mm TPD joints. Statistic results of (c) joint size and (d) grain size in skin and flange at different cases.

5. Conclusions

In this research, a 3D computational fluid dynamic model is employed to study the effect of FSW tool plunge depth on frictional heat, material flow, and microstructure of an AA6068 alloy joint. According to the simulation results and experimental tests, the below conclusions can be presented:

1. The simulation study shows that the axial force and contact area between tools and workpieces increase with increasing TPD. At higher TPD, more pin area penetrates the flange side, and the number of surfaces in contact with the flange and pin increases. Higher axial force and greater contact area between the pin and flange increase the total frictional heat at higher TPD.
2. The heat flux on the flange side is greater than the skin sheet, and at higher TPD, a larger preheat zone is formed in front of the tool in the flange compared to the skin. This phenomenon causes a larger HAZ and TMAZ area in the flange compared to the

- skin for TPD. On the other hand, at higher TPD, larger HAZs and TMAZs are formed on the flange side.
3. TPD affects the stirring of material by affecting the velocity at the interface of the flange and skin. Increasing TPD leads to more stirring action, and at higher TPD, overflow may occur, which leads to material explosion from the joint area and surface flash formation.
 4. Frictional force increases with increasing TPD at the tool–workpiece interface. Higher frictional force significantly increases the velocity of the material behind the welding tool. Low TPD cannot reduce material viscosity, leading to the formation of incomplete joints. Due to the selected range of TPD in this study, the most appropriate joint was obtained at 0.2 mm TPD.

Author Contributions: Conceptualization, S.M. and H.A.D. (Hesamoddin Aghajani Derazkola); methodology, H.A.D. (Hesamoddin Aghajani Derazkola); software, H.A.D. (Hamed Aghajani Derazkola). and A.C.F.; validation, S.M., H.A.D. (Hamed Aghajani Derazkola), and A.C.F.; formal analysis, S.M., H.A.D. (Hamed Aghajani Derazkola), H.A.D. (Hesamoddin Aghajani Derazkola), A.C.F., and D.F.; investigation, S.M., H.A.D. (Hamed Aghajani Derazkola), H.A.D. (Hesamoddin Aghajani Derazkola), and A.C.F.; resources, S.M., H.A.D. (Hamed Aghajani Derazkola), H.A.D. (Hesamoddin Aghajani Derazkola), A.C.F., and D.F.; data curation, H.A.D. (Hesamoddin Aghajani Derazkola); writing—original draft preparation, H.A.D. (Hesamoddin Aghajani Derazkola), A.C.F., and D.F.; writing—review and editing, H.A.D. (Hamed Aghajani Derazkola), A.C.F., and D.F.; visualization, S.M., H.A.D. (Hamed Aghajani Derazkola), and H.A.D. (Hesamoddin Aghajani Derazkola); supervision, H.A.D. (Hamed Aghajani Derazkola); All authors have read and agreed to the published version of the manuscript.

Funding: This research received no external funding.

Institutional Review Board Statement: Not applicable.

Informed Consent Statement: Not applicable.

Data Availability Statement: Data sharing is not applicable to this article.

Conflicts of Interest: The authors declare no conflict of interest.

Abbreviations

Time	t
Coefficient of thermal conductivity	k
Mass-specific heat capacity	c
Density of the materials	ρ
Specific heat	ν
Yield strength	τ
Heat transfer coefficient	he
Initial temperature	Ta
Stefan–Boltzmann constant	B
Emissivity	ε
Convective heat transfer coefficient	ht
Velocity,	s
Welding speed	$S1$
Angular velocity	ω
Axial force	F
Effective strain rate	ε
Material constants	$A = 5.18 \times 10^{10} \text{ S}^{-1}$
Material constants	$a = 1 \text{ MPa}^{-1}$
Material constants	$n = 5.66$
Activation energy	$Q = 158.3 \text{ kJ/mol}$

References

1. Derazkola, H.A.; Khodabakhshi, F. Development of fed friction-stir (FFS) process for dissimilar nanocomposite welding between AA2024 aluminum alloy and polycarbonate (PC). *J. Manuf. Process.* **2020**, *54*, 262–273. [[CrossRef](#)]
2. Derazkola, H.A.; Khodabakhshi, F. A novel fed friction-stir (FFS) technology for nanocomposite joining. *Sci. Technol. Weld. Join.* **2020**, *25*. [[CrossRef](#)]
3. Feistauer, E.E.; Bergmann, L.A.; dos Santos, J.F. Effect of reverse material flow on the microstructure and performance of friction stir welded T-joints of an Al-Mg alloy. *Mater. Sci. Eng. A* **2018**, *731*, 454–464. [[CrossRef](#)]
4. Huang, Y.; Xie, Y.; Meng, X.; Lv, Z.; Cao, J. Numerical design of high depth-to-width ratio friction stir welding. *J. Mater. Process. Technol.* **2018**, *252*, 233–241. [[CrossRef](#)]
5. Konopleva, E.V.; McQueen, H.J.; Evangelista, E. Serrated grain boundaries in hot-worked aluminum alloys at high strains. *Mater. Charact.* **1995**, *34*, 251–264. [[CrossRef](#)]
6. Mehta, K.P.; Patel, R.; Vyas, H.; Memon, S.; Vilaça, P. Repairing of exit-hole in dissimilar Al-Mg friction stir welding: Process and microstructural pattern. *Manuf. Lett.* **2020**, *23*, 67–70. [[CrossRef](#)]
7. Memon, S.; Paidar, M.; Mehta, K.P.; Babaei, B.; Lankarani, H.M. Friction Spot Extrusion Welding on Dissimilar Materials AA2024-T3 to AA5754-O: Effect of Shoulder Plunge Depth. *J. Mater. Eng. Perform.* **2021**, *30*, 334–345. [[CrossRef](#)]
8. Paidar, M.; Mehrez, S.; Babaei, B.; Memon, S.; Ojo, O.O.; Lankarani, H.M. Dissimilar welding of AA5083 to AZ31 Mg alloys using modified friction stir clinching brazing. *Mater. Lett.* **2021**, 129764. [[CrossRef](#)]
9. Memon, S.; Paidar, M.; Mehrez, S.; Cooke, K.; Ojo, O.O.; Lankarani, H.M. Effects of materials positioning and tool rotational speed on metallurgical and mechanical properties of dissimilar modified friction stir clinching of AA5754-O and AA2024-T3 sheets. *Results Phys.* **2021**, *22*, 103962. [[CrossRef](#)]
10. Paidar, M.; Memon, S.; Samusenkov, V.O.; Babaei, B.; Ojo, O.O. Friction spot extrusion welding-brazing of copper to aluminum alloy. *Mater. Lett.* **2021**, *285*, 129160. [[CrossRef](#)]
11. Mirzaei, M.; Asadi, P.; Fazli, A. Effect of Tool Pin Profile on Material Flow in Double Shoulder Friction Stir Welding of AZ91 Magnesium Alloy. *Int. J. Mech. Sci.* **2020**, *183*, 105775. [[CrossRef](#)]
12. Janeczek, A.; Tomków, J.; Fydrych, D. The Influence of Tool Shape and Process Parameters on the Mechanical Properties of AW-3004 Aluminium Alloy Friction Stir Welded Joints. *Materials* **2021**, *14*, 3244. [[CrossRef](#)] [[PubMed](#)]
13. Memon, S.; Murillo-Marrodán, A.; Lankarani, H.M.; Aghajani Derazkola, H. Analysis of Friction Stir Welding Tool Offset on the Bonding and Properties of Al-Mg-Si Alloy T-Joints. *Materials* **2021**, *14*, 3604. [[CrossRef](#)] [[PubMed](#)]
14. Donati, L.; Tomesani, L.; Morri, A. Structural T-joint produced by means of friction stir welding (FSW) with filling material. *Int. J. Mater. Form.* **2009**, *2*, 295. [[CrossRef](#)]
15. Buffa, G.; Fratini, L.; Micari, F.; Shivpuri, R. Material Flow in FSW of T-joints: Experimental and Numerical Analysis. *Int. J. Mater. Form.* **2008**, *1*, 1283–1286. [[CrossRef](#)]
16. Su, Y.; Li, W.; Liu, X.; Gao, F.; Yu, Y.; Vairis, A. Strengthening mechanism of friction stir welded alpha titanium alloy specially designed T-joints. *J. Manuf. Process.* **2020**, *55*, 1–12. [[CrossRef](#)]
17. Derazkola, H.A.; Aval, H.J.; Elyasi, M. Analysis of process parameters effects on dissimilar friction stir welding of AA1100 and A441 AISI steel. *Sci. Technol. Weld. Join.* **2015**, *20*. [[CrossRef](#)]
18. Dehghani, M.; Amadeh, A.; Akbari Mousavi, S.A.A. Investigations on the effects of friction stir welding parameters on inter-metallic and defect formation in joining aluminum alloy to mild steel. *Mater. Des.* **2013**, *49*, 433–441. [[CrossRef](#)]
19. Salloomi, K.N. Fully coupled thermomechanical simulation of friction stir welding of aluminum 6061-T6 alloy T-joint. *J. Manuf. Process.* **2019**, *45*, 746–754. [[CrossRef](#)]
20. Derazkola, H.A.; Kashiry Fard, R.; Khodabakhshi, F. Effects of processing parameters on the characteristics of dissimilar friction-stir-welded joints between AA5058 aluminum alloy and PMMA polymer. *Weld. World* **2018**, *62*. [[CrossRef](#)]
21. Eyvazian, A.; Hamouda, A.M.; Aghajani Derazkola, H.; Elyasi, M. Study on the effects of tool tilt angle, offset and plunge depth on friction stir welding of poly(methyl methacrylate) T-joint. *Proc. Inst. Mech. Eng. Part B J. Eng. Manuf.* **2020**, 234. [[CrossRef](#)]
22. Safeen, M.W.; Russo Spena, P. Main Issues in Quality of Friction Stir Welding Joints of Aluminum Alloy and Steel Sheets. *Metals* **2019**, *9*, 610. [[CrossRef](#)]
23. Hasan, A.F.; Bennett, C.J.; Shipway, P.H. A numerical comparison of the flow behaviour in Friction Stir Welding (FSW) using unworn and worn tool geometries. *Mater. Des.* **2015**, *87*, 1037–1046. [[CrossRef](#)]
24. Su, H.; Wu, C. Numerical Simulation for the Optimization of Polygonal Pin Profiles in Friction Stir Welding of Aluminum. *Acta Metall. Sin. Engl. Lett.* **2021**. [[CrossRef](#)]
25. Wang, X.; Gao, Y.; Liu, X.; McDonnell, M.; Feng, Z. Tool-workpiece stick-slip conditions and their effects on torque and heat generation rate in the friction stir welding. *Acta Mater.* **2021**, *213*, 116969. [[CrossRef](#)]
26. Aghajani Derazkola, H.; Garcia, E.; Elyasi, M. Underwater friction stir welding of PC: Experimental study and thermo-mechanical modelling. *J. Manuf. Process.* **2021**, *65*, 161–173. [[CrossRef](#)]
27. Iqbal, M.P.; Tripathi, A.; Jain, R.; Mahto, R.P.; Pal, S.K.; Mandal, P. Numerical modelling of microstructure in friction stir welding of aluminium alloys. *Int. J. Mech. Sci.* **2020**, *185*, 105882. [[CrossRef](#)]
28. Zhao, W.; Wu, C.; Shi, L. Acoustic induced antifriction and its effect on thermo-mechanical behavior in ultrasonic assisted friction stir welding. *Int. J. Mech. Sci.* **2021**, *190*, 106039. [[CrossRef](#)]

29. Li, X.; Hou, L.; Wei, Y.; Wei, Z. Constitutive Equation and Hot Processing Map of a Nitrogen-Bearing Martensitic Stainless Steel. *Metals* **2020**, *10*, 1502. [[CrossRef](#)]
30. Muhammad, N.A.; Wu, C. Evaluation of capabilities of ultrasonic vibration on the surface, electrical and mechanical behaviours of aluminium to copper dissimilar friction stir welds. *Int. J. Mech. Sci.* **2020**, *183*, 105784. [[CrossRef](#)]
31. Hernández, C.A.; Ferrer, V.H.; Mancilla, J.E.; Martínez, L.C. Three-dimensional numerical modeling of the friction stir welding of dissimilar steels. *Int. J. Adv. Manuf. Technol.* **2017**, *93*, 1567–1581. [[CrossRef](#)]
32. Lambiase, F.; Derazkola, H.A.; Simchi, A. Friction Stir Welding and Friction Spot Stir Welding Processes of Polymers—State of the Art. *Materials* **2020**, *13*, 2291. [[CrossRef](#)]
33. Robe, H.; Claudin, C.; Bergheau, J.-M.; Feulvarch, E. R-ALE simulation of heat transfer during friction stir welding of an AA2xxx/AA7xxx joint on a large process window. *Int. J. Mech. Sci.* **2019**, *155*, 31–40. [[CrossRef](#)]
34. Rana, P.K.; Narayanan, R.G. Numerical and experimental response of FSSW of AA5052-H32/epoxy/AA5052-H32 sandwich sheets with varying core properties. *Int. J. Mater. Form.* **2020**. [[CrossRef](#)]
35. Yu, P.; Wu, C.; Shi, L. Analysis and characterization of dynamic recrystallization and grain structure evolution in friction stir welding of aluminum plates. *Acta Mater.* **2021**, *207*, 116692. [[CrossRef](#)]
36. Yang, H.; Zhao, H.; Xu, X.; Zhou, L.; Zhao, H.; Liu, H. Effect of Stirring Pin Rotation Speed on Microstructure and Mechanical Properties of 2A14-T4 Alloy T-Joints Produced by Stationary Shoulder Friction Stir Welding. *Materials* **2021**, *14*, 1938. [[CrossRef](#)]
37. Aghajani Derazkola, H.; Kordani, N.; Aghajani Derazkola, H. Effects of friction stir welding tool tilt angle on properties of Al-Mg-Si alloy T-joint. *CIRP J. Manuf. Sci. Technol.* **2021**, *33*, 264–276. [[CrossRef](#)]
38. Aghajani Derazkola, H.; Simchi, A. Experimental and thermomechanical analysis of friction stir welding of poly(methyl methacrylate) sheets. *Sci. Technol. Weld. Join.* **2017**. [[CrossRef](#)]
39. Fratini, L.; Buffa, G.; Micari, F.; Shivpuri, R. On the material flow in FSW of T-joints: Influence of geometrical and technological parameters. *Int. J. Adv. Manuf. Technol.* **2009**, *44*, 570–578. [[CrossRef](#)]
40. Gale, W.F.; Totemeier, T. Diffusion in metals. In *Smithells Metals Reference Book*, 8th ed.; Butterworth-Heinemann: Oxford, UK, 2004; pp. 13–120; ISBN 978-0-7506-7509-3.
41. Gale, W.F.; Totemeier, T. Gas–metal systems. In *Smithells Metals Reference Book*, 8th ed.; Butterworth-Heinemann: Oxford, UK, 2004; pp. 12–28; ISBN 978-0-7506-7509-3.
42. Gale, W.F.; Totemeier, T. General physical properties. In *Smithells Metals Reference Book*, 8th ed.; Butterworth-Heinemann: Oxford, UK, 2004; pp. 14–45; ISBN 978-0-7506-7509-3.
43. Gale, W.F.; Totemeier, T. General physical and chemical constants. In *Smithells Metals Reference Book*, 8th ed.; Butterworth-Heinemann: Oxford, UK, 2004; pp. 3–11; ISBN 978-0-7506-7509-3.
44. Dialami, N.; Cervera, M.; Chiumenti, M. Effect of the Tool Tilt Angle on the Heat Generation and the Material Flow in Friction Stir Welding. *Metals* **2019**, *9*, 28. [[CrossRef](#)]
45. Akram, J.; Puli, R.; Kalvala, P.R.; Misra, M. A novel weld transition joint by friction surfacing. *Manuf. Lett.* **2014**, *2*, 104–107. [[CrossRef](#)]
46. Chen, F.; Cui, Z.; Liu, J.; Zhang, X.; Chen, W. Modeling and simulation on dynamic recrystallization of 30Cr2Ni4MoV rotor steel using the cellular automaton method. *Model. Simul. Mater. Sci. Eng.* **2009**, *17*, 75015. [[CrossRef](#)]
47. Tanaka, T.; Nezu, M.; Uchida, S.; Hirata, T. Mechanism of intermetallic compound formation during the dissimilar friction stir welding of aluminum and steel. *J. Mater. Sci.* **2020**, *55*, 3064–3072. [[CrossRef](#)]
48. Chitturi, V.; Pedapati, S.R.; Awang, M. Effect of Tilt Angle and Pin Depth on Dissimilar Friction Stir Lap Welded Joints of Aluminum and Steel Alloys. *Materials* **2019**, *12*, 3901. [[CrossRef](#)] [[PubMed](#)]
49. Talebizadehsardari, P.; Musharavati, F.; Khan, A.; Sebaey, T.A.; Eyvaziana, A.; Derazkola, H.A. Underwater friction stir welding of Al-Mg alloy: Thermo-mechanical modeling and validation. *Mater. Today Commun.* **2021**, *26*, 101965. [[CrossRef](#)]
50. Mahto, R.P.; Gupta, C.; Kinjawadekar, M.; Meena, A.; Pal, S.K. Weldability of AA6061-T6 and AISI 304 by underwater friction stir welding. *J. Manuf. Process.* **2019**, *38*, 370–386. [[CrossRef](#)]
51. Papahn, H.; Bahemmat, P.; Haghpanahi, M.; Sommitsch, C. Study on governing parameters of thermal history during underwater friction stir welding. *Int. J. Adv. Manuf. Technol.* **2015**, *78*, 1101–1111. [[CrossRef](#)]
52. Reddy, V.V.; Kumar, A.; Valli, P.M.; Reddy, C.S. Influence of surfactant and graphite powder concentration on electrical discharge machining of PH17-4 stainless steel. *J. Braz. Soc. Mech. Sci. Eng.* **2015**, *37*, 641–655. [[CrossRef](#)]
53. Śniezek, L.; Kosturek, R.; Wachowski, M.; Kania, B. Microstructure and Residual Stresses of AA2519 Friction Stir Welded Joints under Different Heat Treatment Conditions. *Materials* **2020**, *13*, 834. [[CrossRef](#)]
54. Sun, Z.; Wu, C.S. Influence of tool thread pitch on material flow and thermal process in friction stir welding. *J. Mater. Process. Technol.* **2020**, *275*, 116281. [[CrossRef](#)]
55. Guan, M.; Wang, Y.; Huang, Y.; Liu, X.; Meng, X.; Xie, Y.; Li, J. Non-weld-thinning friction stir welding. *Mater. Lett.* **2019**, *255*, 126506. [[CrossRef](#)]
56. Miyamori, T.; Sato, Y.; Kokawa, H. *Influence of Underwater Operation on Friction Stir Welding of Medium Carbon Steel BT—Friction Stir Welding and Processing IX*; Hovanski, Y., Mishra, R., Sato, Y., Upadhyay, P., Yan, D., Eds.; Springer International Publishing: Cham, Switzerland, 2017; pp. 23–28.

57. Bhattacharya, T.K.; Das, H.; Pal, T.K. Influence of welding parameters on material flow, mechanical property and intermetallic characterization of friction stir welded AA6063 to HCP copper dissimilar butt joint without offset. *Trans. Nonferrous Met. Soc. China* **2015**, *25*, 2833–2846. [[CrossRef](#)]
58. Deng, Y.; Qiu, Z.; Zuo, D.; Zeng, J.; Zhang, W. Influence of tool offset on microstructure and properties of Mg/Al dissimilar alloys by friction stir welding joints at low heat input. *Int. J. Adv. Manuf. Technol.* **2020**, *109*, 2845–2853. [[CrossRef](#)]
59. Đurđević, A.; Sedmak, A.; Živković, A.; Đurđević, Đ.; Marković, M.; Milčić, M. Microhardness and Macrostructures of Friction Stir Welded T-joints. *Procedia Struct. Integr.* **2018**, *13*, 424–429. [[CrossRef](#)]
60. Buffa, G.; Fratini, L.; Impero, F.; Masnata, A.; Scherillo, F.; Squillace, A. Surface and mechanical characterization of stationary shoulder friction stir welded lap joints: Experimental and numerical approach. *Int. J. Mater. Form.* **2020**, *13*, 725–736. [[CrossRef](#)]
61. Jesus, J.S.; Costa, J.M.; Loureiro, A.; Ferreira, J.M. Assessment of friction stir welding aluminium T-joints. *J. Mater. Process. Technol.* **2018**, *255*, 387–399. [[CrossRef](#)]
62. Aghajani Derazkola, H.; García, E.; Eyvazian, A.; Aberoumand, M. Effects of Rapid Cooling on Properties of Aluminum-Steel Friction Stir Welded Joint. *Materials* **2021**, *14*, 908. [[CrossRef](#)]
63. Jabraeili, R.; Jafarian, H.R.; Khajeh, R.; Park, N.; Kim, Y.; Heidarzadeh, A.; Eivani, A.R. Effect of FSW process parameters on microstructure and mechanical properties of the dissimilar AA2024 Al alloy and 304 stainless steel joints. *Mater. Sci. Eng. A* **2021**, *814*, 140981. [[CrossRef](#)]
64. Mehtonen, S.V.; Karjalainen, L.P.; Porter, D.A. Hot deformation behavior and microstructure evolution of a stabilized high-Cr ferritic stainless steel. *Mater. Sci. Eng. A* **2013**, *571*, 1–12. [[CrossRef](#)]
65. Kumar, S.S.; Murugan, N.; Ramachandran, K.K. Effect of tool tilt angle on weld joint properties of friction stir welded AISI 316L stainless steel sheets. *Measurement* **2020**, *150*, 107083. [[CrossRef](#)]
66. Hou, X.; Yang, X.; Cui, L.; Zhou, G. Influences of joint geometry on defects and mechanical properties of friction stir welded AA6061-T4 T-joints. *Mater. Des.* **2014**, *53*, 106–117. [[CrossRef](#)]
67. Kaushik, P.; Dwivedi, D.K. Effect of tool geometry in dissimilar Al-Steel Friction Stir Welding. *J. Manuf. Process.* **2020**. [[CrossRef](#)]

